# Monitoring Preferential Flow of Water in Sand Using Thermoacoustics Wave Imaging

Chang Liu[1], Xu Mao[2], Chang Wang[1], Rebecca Liyanage[3], Juan Heredia-Juesas[1], Ruben Juanes[4], and Jose Martinez-Lorenzo[1]

[1]Northeastern University
[2]China Agricultural University
[3]MIT
[4]Massachusetts Institute of Techonology

December 22, 2022

## Abstract

Accurate predictions of fluid flow, mass transport, and reaction rates critically impact the efficiency and reliability of subsurface exploration and sustainable use of subsurface resources. Quantitative dynamical sensing and imaging can play a pivotal role in the ability to make such predictions. Geophysical thermoacoustic technology has the potential to provide the aforementioned capabilities since it builds upon the principle that electromagnetic and mechanical wave fields can be coupled through a thermodynamic process. In this letter, we present laboratory experiments featuring the efficacy of thermoacustic imaging in the monitoring of preferential flow of water in porous media. Our laboratory experimental equipment can be readily packaged in a form factor that fits in a borehole, and the use of multiple acoustic transducers—which can be combined with volumetric coding techniques—has the potential to provide quasi-real-time imaging (0.5 Hertz video rate) of regions in close proximity (a few meters) of an open field well.

# Monitoring Preferential Flow of Water in Sand Using Thermoacoustics Wave Imaging

**Chang Liu [1], Xu Mao [1], Chang Wang [1], Rebecca Liyanage [2], Juan Heredia Juesas [1,3], Ruben Juanes [2], Jose Angle Martinez-Lorenzo [1,3]**

[1]Department of Mechanical and Industrial Engineering, Northeastern University, Boston, Massachusetts, 02115
[2]Department of Civil and Environmental Engineering, Massachusetts Institute of Technology, Cambridge, Massachusetts, 02139
[3]Department of Electrical and Computer Engineering, Northeastern University, Boston, Massachusetts, 02115

**Key Points:**

- The relationship between water saturation in sand and the resultant thermoacoustics wave amplitude is monotonic.
- The reconstructed thermoacoustics images match well with the optical ground truth for water-saturated sand.
- Thermoacoustics imaging enables real-time monitoring of water distribution in subsurface sand.

Corresponding author: Chang Liu, liu.chang4@northeastern.edu

Corresponding author: Jose Angel Martinez-Lorenzo, j.martinez-lorenzo@northeastern.edu

**Abstract**

Accurate predictions of fluid flow, mass transport, and reaction rates critically impact the efficiency and reliability of subsurface exploration and sustainable use of subsurface resources. Quantitative dynamical sensing and imaging can play a pivotal role in the ability to make such predictions. Geophysical thermoacoustic technology has the potential to provide the aforementioned capabilities, since it builds upon the principle that electromagnetic and mechanical wave fields can be coupled through a thermodynamic process. In this letter, we present laboratory experiments featuring the efficacy of thermoacustic imaging in the monitoring of preferential flow of water in porous media. Our laboratory experimental equipment can be readily packaged in a form factor that fits in a borehole, and the use of multiple acoustic transducers—which can be combined with volumetric coding techniques—has the potential to provide quasi-real-time imaging (0.5 Hertz video rate) of regions in close proximity (a few meters) of an open field well.

## Plain Language Summary

Multiphysics subsurface sensing and imaging technology has the potential to provide unique insights to better understand multiphase flow and transport in porous media in 4D (time and space). Conventional high-resolution, laboratory-based imaging technology—such as X-ray or MRI—require power-hungry and often bulky equipment; the latter limits their use in open field experiments and challenges their ability to perform real-time image reconstruction. Acoustics Doppler imaging has been used for real-time flow velocity monitoring in biomedical applications; however, the relationship between fluid saturation in porous media and measured acoustic pressure still requires further investigation. In this letter we show how microwave-induced thermoacoustic (TA) imaging technology can be applied to monitor water distribution in sand. In contrast to traditional acoustic imaging, the proposed TA method exhibits a dominant monotonic relationship between the degree of water saturation and the measured amplitude of the TA pressure. Our experimental results show the efficacy of TA technology for imaging 2D water distribution profiles in sand. The reconstructed TA images are in good agreement with the optical ground truth water distribution map, thus illustrating the feasibility of the proposed method for real-world field applications in agricultural and hydrological sciences.

## 1 Introduction

Understanding the distribution of fluid phases during multiphase flow in porous media is critical in a wide array of subsurface natural processes and engineering applications (Jarvis, 2007; Blunt et al., 2013; Berg et al., 2013). Optical imaging, X-ray tomography, and magnetic resonance imaging (MRI) are just a few of the most commonly used non-invasive, high-resolution imaging techniques (Katuwal et al., 2018; Pohlmeier et al., 2018; Cnudde & Boone, 2013). However, these methods are subject to important drawbacks that not only limit their use in field applications but also in controlled laboratory environments (Werth et al., 2010; Wildenschild et al., 2002). Optical imaging techniques are well suited to reconstruct fluid distribution in a real-time fashion; however, their use is mostly limited to 2D geometries due reduced penetration on light in highly opaque media and fluid saturation cannot be easily quantified (Moebius & Or, 2012; Roman et al., 2020), although advances such as refraction-index matching, planar laser-induced fluorescence and confocal microscopy have extended the range of application of 3D optical (Kong et al., 2011; Sharma et al., 2011; Krummel et al., 2013; Dalbe & Juanes, 2018). In contrast, X-ray and MRI methods can provide a quantified high-resolution image of 3D geometries (Pohlmeier et al., 2018; Liyanage et al., 2019); however, these methods are limited in their ability to capture the transient behavior of fast fluid flow due to its intrinsic slow scanning speed (Luo et al., 2008; Koestel & Larsbo, 2014). For example, preferential flow, which refers to the phenomenon of channeling in-filtrating water as a result of 'macropores' (Beven & Germann, 1982) or gravitational instability (Glass et al., 1989; Wei et al., 2014; Liyanage & Juanes, 2021), can reach a wetting front velocity up several millimeters per second, calling for a real-time imaging method in 3D (Zhang et al., 2018; Jarvis et al., 2016; Beven & Germann, 2013).

Acoustic (AC) and seismic waves are commonly used for subsurface situational awareness (Müller et al., 2012; David et al., 2015); however, the intrinsic relationship between acoustic properties of rocks and fluid saturation remains poorly understood. Nevertheless, it has been shown that an increase in water saturation modulates the amplitude of P-waves, which ultimately gives form to the acoustics signature of heterogeneous mixtures of rocks and fluids (Pimienta et al., 2019; David et al., 2017). While ultrasound imaging has been applied in geophysics, the vague relationship between the morphology of the sample under test and ultrasound image suggests that further advances are needed before this methodology can be used in quantitative dynamical imaging applications (Zou et al., 2016, 2018).

TA sensing and imaging presents a new opportunity to better characterize the subsurface due to its inherent multiphysics nature, in which elastic waves are created due to the thermal expansion and contraction of a target when it is illuminated by a high intensity microwave source (Liu et al., 2018). This technology, originally used for breast cancer detection, leverages on the high contrast existing between healthy and cancerous tissues at microwaves frequencies and the high resolution of AC technology to create images with a pixel resolution of tens of micrometers (Lou et al., 2012). Such a thermodynamics-driven coupling of electromagnetic and mechanical waves overcomes the intrinsic poor resolution of electromagnetic images and the low contrast of AC images when used in a standalone fashion (Cui et al., 2017; Xu & Wang, 2006). At particular spatial scales, there are certain similarities amongst the constitutive properties of biological and geological materials—suggesting that TA technology may be used for geophysical imaging applications. The latter assumption was experimentally tested and validated in (Liu et al., 2019); the authors demonstrated that geological materials, such as sand and rocks, can indeed generate detectable TA pressure waves. Moreover, the significant contrast existing between the dielectric constants of water and quartz sand enables the monitoring of fluid distribution in sandy environments.

Conventional real-time imaging systems use arrays of transducers, often involving over 100 receivers, to collect large amounts of information in a reduced amount of time; however, these bulky, power-hungry, and often expensive devices constrain the use of TA imaging in open field scenarios (Yin et al., 2004). TA technology is well poised to enable real-time imaging while using a reduced number of receivers. The latter is afforded by performing volumetric spatial coding of the wave fields (Lorenzo et al., 2015) to maximize the sensing capacity of the imaging system, which is defined as the information-transfer efficiency between imaging domain and the measured data. Volumetric coding can be performed using artificial metamaterials, holey cavities, and compressive reflectors; this reduces the mutual information among successive measurements and increase the sensing capacity of the imaging system (Mao et al., 2020).

In this letter we present the first study showing the efficacy of microwave-induced thermoacoustics imaging to monitor fluid distribution in geological media. This technique has the potential to offer real-time reconstruction of fluid flow in 4D, at distance, and using non-contact sensors—an ability that could prove instrumental to extend our understanding of water distribution and heterogeneous infiltration in the Earth's critical zone (Richter & Mobley, 2009). This letter is structured as follows: In Section 2 we introduce the background theory of applying TA waves to monitor water distribution in sand. Based on this, we establish a simulation model to predict the relationship between water saturation and the TA signal strength. We design an experiment to validate this principle. In Section 3, we analyze the data from the simulation and experiment, both showing a monotonic relationship between water saturation and TA signal amplitude.

Table 1: Material properties used in simulation

| Material | $\epsilon_r$ | $\sigma$ [S/m] | $\rho$ [kg/m$^3$] | $\kappa$ [GPa] | $\beta$ [$10^{-6}$/K] | $C_p$ [J/(kg· K)] |
|---|---|---|---|---|---|---|
| Quartz Sand | 4.27 | 0 | 2650 | 37 | 1 | 743 |
| Water | 80 | 0.05 | 1000 | 2.25 | 210 | 4180 |
| Air | 1 | 0 | - | - | - | - |
| Oil | 2.6 | 0.01 | - | - | - | - |
| Acrylic Sheet | 3.4 | $6.7 \times 10^{-15}$ | - | - | - | - |

In Section 4 we present the experimental results of recovering the water distribution profile in a quasi-3D sand cell (in which one dimension is smaller than the other two), and in Section 5 we summarize the main outcomes of our study.

## 2 Materials and Methods

Microwave induced TA pressure waves are generated due to the thermal expansion of an object when it is illuminated by a short, intense microwave pulse. The governing equations for TA wave are:

$$\nabla^2 p(\mathbf{r},t) - \frac{1}{c^2(\mathbf{r})}\frac{\partial^2}{\partial t^2}p(\mathbf{r},t) = -\frac{\beta(\mathbf{r})}{C_p(\mathbf{r})}\frac{\partial Q(\mathbf{r},t)}{\partial t} \tag{1a}$$

$$Q(\mathbf{r},t) \approx \sigma(\mathbf{r})||E(\mathbf{r})||^2 f^2(t) \tag{1b}$$

where $p(\mathbf{r},t)$ is the pressure, $c(\mathbf{r})$ is the sound speed, $\beta(\mathbf{r})$ is the thermal expansion rate, $C_p(\mathbf{r})$ is the heat capacity, and $Q(\mathbf{r},t)$ is the heat source. This term is defined in Eq. (1b), where $\sigma(\mathbf{r})$ is the electric conductivity, $\mathbf{E}(\mathbf{r})$ is the electric field, and $f(t)$ is the excitation pulse function. According to Eq. (1b), the right hand side of Eq. (1a) can be written as $-\frac{\beta(\mathbf{r})}{C_p(\mathbf{r})}\sigma(\mathbf{r})||E(\mathbf{r})||^2\frac{\partial}{\partial t}f^2(t)$. This term can be decomposed as the product of two functions: one is a time varying modulating signal $\frac{\partial}{\partial t}f^2(t)$; and the other is a material-dependent space varying distribution $S(\mathbf{r}) = -\frac{\beta(\mathbf{r})}{C_p(\mathbf{r})}\sigma(\mathbf{r})||E(\mathbf{r})||^2$. The constitutive properties within the source term $S(\mathbf{r})$ are affected by the water saturation of the sandy porous medium, and their value can be approximated by empirical rock physics models (RPMs). The latter provides an estimation of the constitutive properties of the compound mixture and the volume fraction of each one of its individual components.

Our first experiment is aimed at the computational modeling and experimental testing of the effect of water saturation on the signal strength. A multiphysics engine (Inc., 2020) was used to reveal such relationship. Figure 1a displays the baseline geometry of the simulation; the material properties are predicted using the RPMs described in (Shen et al., 1985; Troschke & Burkhardt, 1998; Waples & Waples, 2004) and summarized in Table 1—where $\epsilon_r$ is the relative permittivity, $\rho$ is the density, and $\kappa$ is the bulk modulus. TA pressure signals as well as the source strength predicted by the computational models are contrasted with those experimentally measured in the first of our TA imaging testbeds. Six sand samples having different quantitatively-controlled saturation levels are prepared for the experiment.

The second experiment is aimed at demonstrating that TA imaging can effectively be used to monitor fingered water infiltration in a quasi-3D sand cell. The testbed is shown in Fig. 1c. Since only one transducer is applied in the experiment, the sand cell with static water distribution is imaged.

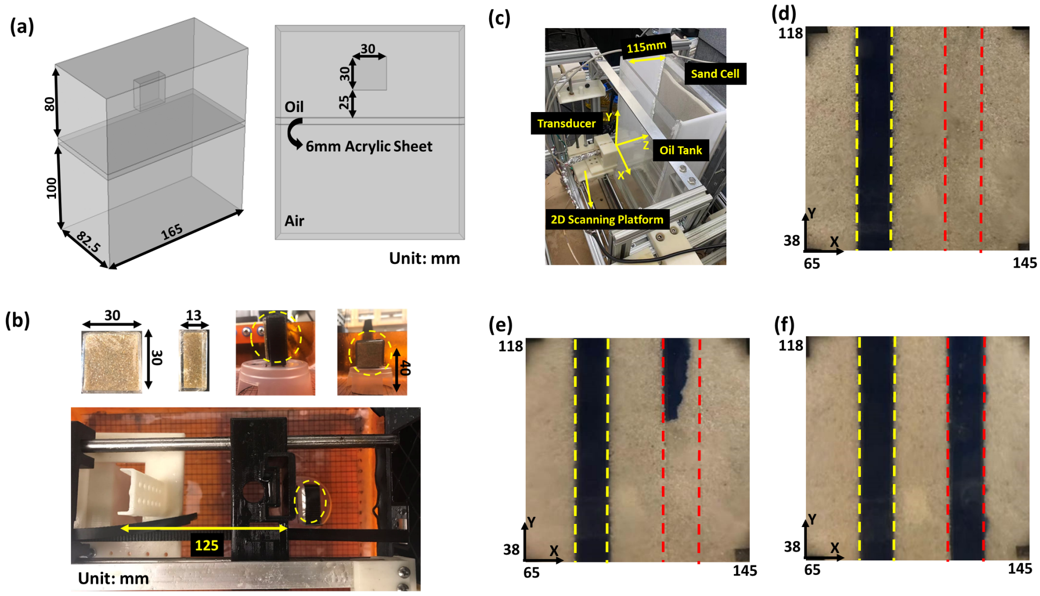


Figure 1: Monitoring water distribution profile in sand using the TA wave: (a) RPM-driven simulation geometry, (b) the testbed for the first experiment, (c) the testbed for the second experiment, (d) water distribution inside the marker, (e) water distribution after the first injection, and (f) water distribution after the second injection.

## 3 Data Collection

In the first experiment, a plastic box with one facet removed is filled with 12.5g of sand (#20 graded). The size of the sand box is 30mm×30mm×13mm, as shown in Fig. 1b. While keeping the dry sample for comparison, the other five samples are injected with different amounts of water: 0.7g, 1.4g, 2.1g, 2.8g, and 3.5g, separately. Provided that the porosity of sand sample is $\Phi = 30\%$, this results in water saturations of 20%, 40%, 60%, 80%, and 100% for each sample, respectively. Later, the sand box is sealed with a thin layer of plastic wrap and black waterproof tape. Finally, the sand box is held still for 1 hour to allow for the water to spread through the sample, since the water is injected from the opening facet of the sample. As it can be seen in Fig. 1b, the sand sample is placed parallel to the transducer in the oil bath at a distance of 125mm away from the transducer. Moreover, the center of the sand sample is lifted 40mm to match the height of the transducer. After one measurement is finished, the previous sand box is replaced with another sand sample with different saturation level.

In the second experiment, the quasi-3D sand cell (10mm thickness) is separated from the acoustic transducer by an oil tank. The distance between the sand cell and the transducer is 115mm. The sand sample under test is geometrically constrained to a small narrow region using a plastic enclosure, and two such enclosures are prepared: the left one is fully saturated as the marker for reference (yellow dashed line in Fig. 1d), and the right one is for dynamic water distribution imaging (red dashed line in Fig. 1d). In the first part of this experiment, 1.5mL of blue-dyed water is injected from the top into the right enclosure, which is shown in Fig. 1e. In the second part of this experiment, additional amount of 3.9mL of blue-dyed water is injected into the right enclosure, and the final water distribution is shown in Fig. 1f. In this experiment, the selected imaging area ranges from X = 65mm to X = 145mm, Y = 38mm to Y = 118mm, and Z = 100mm to Z = 140mm. The scanning range of transducer is slightly larger than the imaging area to achieve

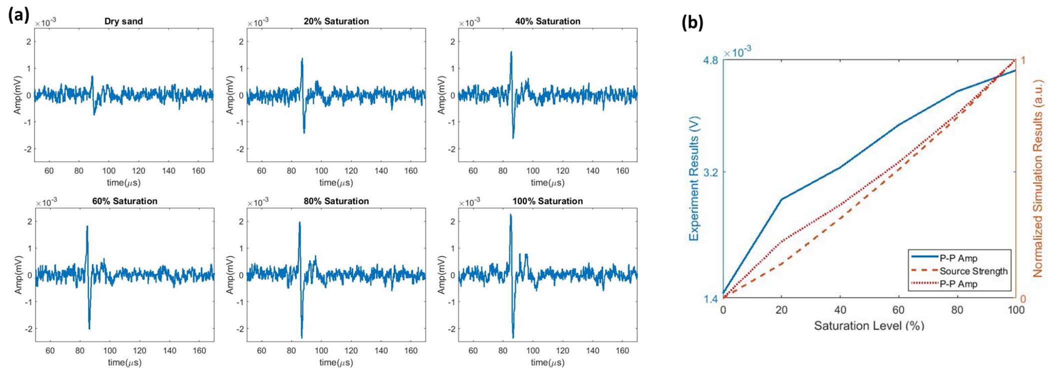


Figure 2: The monotonic relationship between water saturation and the TA amplitude: (a) measured signals of the sand box saturated by different amount of water, and (b) the peak-peak amplitude of the collected signals (solid line), the simulated source strength (dashed line) and the peak-peak amplitude (dotted line) after normalization.

better resolution in X-Y plane, ranging from X = 53mm to X = 157mm in X-direction and Y = 26mm to Y = 130mm in Y-direction. The raster scan is conducted four times: dry sand, after the preparation of the marker, after the first injection and after the second injection into the right enclosure. Moreover, to guarantee the fully spread of water, the raster scan starts after the water profile stops moving. The measurements are collected with 4mm spatial separation for every measured point, thus making a total number of 729 measurements for each scan. During these scans, the power of the EM wave remains constant, and the difference between the successive measurements should be the effect of the injected water.

## 4 Results

In the first experiment, the collected TA signals for samples with different water saturations are plotted in Fig. 2a. As it can be seen, the amplitudes of the measured signals depend on the amount of water in the sand. The peak-peak value of those signals are plotted in Fig. 2b, and the simulated source strengths as well as the peak-peak amplitudes are also shown for comparison after normalization. Several points in Fig. 2b deserve discussion. All results in Fig. 2b exhibit a strictly monotonic relationship between the TA signal amplitude with the amount of injected water, which reveals the feasibility of distinguishing the water saturation in sand using TA waves. The simulated results of peak-peak amplitude and source strength both show a nearly linear relationship against the saturation level, which can be used as a prediction for the water saturation level in the following experiment. We also observe that the dry sand can transmit a detectable TA wave in the experiment while the simulation result shows a zero source strength. This is because the sand used in the experiment is not fully dehydrated. Furthermore, the trend of the experimental measurements exhibit a reversed curvature when compared to that of the simulated results, which may be attributed to by several factors. Firstly, the numerical simulation considers the sample to have a homogeneous distribution of water saturation; while the experiment may have a heterogeneous one due to the water injection in the open facet of the box. Secondly, there may exist important differences between the material properties predicted by the selected RPM and the sand sample used in the experiment.

In the second experiment, the left enclosure, as shown in Fig. 1d, is fully saturated to determine the saturation level of the dynamic water distribution inside the right en-

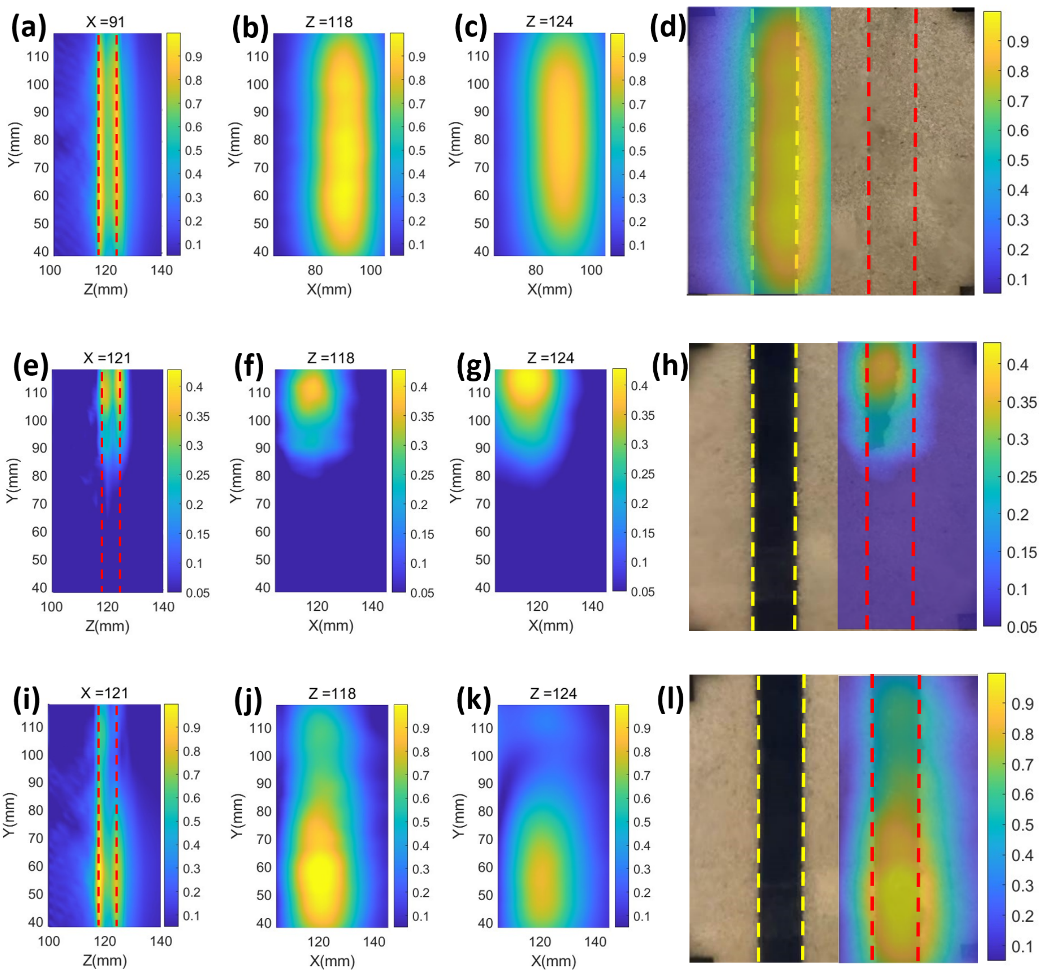


Figure 3: Water distribution reconstruction using the TA waves: (a) slice taken at X = 91mm for marker, (b) slice taken at Z = 118mm for marker, (c) slice taken at Z = 124mm for marker, (d) overlapping marker image with ground truth, (e) slice taken at X = 121mm for the first injection, (f) slice taken at Z = 118mm for the first injection, (g) slice taken at Z = 124mm for the first injection, (h) overlapping the first injection image with ground truth, (i) slice taken at X = 121mm for the second injection, (j) slice taken at Z = 118mm for the second injection, (k) slice taken at Z = 124mm for the second injection, and (l) overlapping the second injection image with ground truth.

closure based on the simulated results presented in the first experiment. The images after first infiltration—Fig. 1e—show that the color intensity of the fluid map is mainly remained on the top. Moreover, the fluid distribution after the second injection has spread to the whole area of the enclosure compared with the first injection. This visual information is used as optical ground truth to drive the comparison with the TA image.

Figure 3a presents the imaging result of a cross section (X = 91mm) for the marker area, which shows the capability of TA imaging to recover subsurface information of the sandy medium. It is noteworthy that the position of the selected cross section is not at the center of the imaging area but, rather, at the center of the marker area. As shown in Fig. 3a, the intensity of the image stays constant from top to the bottom of the enclosure, in agreement with the optical ground truth of Fig. 1d. Furthermore, the first peak appears at Z = 118mm and the second peak appears at Z = 124mm in the image, corresponding to the front and back boundary of the sand cell, individually. In addition, the image strength at the first and second peaks is similar because the EM wave is transmitted from the back (negative X direction), which partly compensates for the attenuation effect. The reconstructed images of the water infiltration profile in the X-Y plane are shown in Figs. 3b and 3c, which correspond to the slice taken at Z = 118mm and Z = 124mm, respectively. Both recovered images show an uniform distribution inside the area of the enclosure. Figure 3d overlaps the ground truth of marker with the front boundary image. Figures 3e-h present the imaging results after the first injection. In contrast with Fig. 3a, the image strength in Fig. 3e stays on the top part of the enclosure, which agrees with the ground truth in Fig. 3h. Compared with those results of the first injection, the recovered images for the second injection in Figs. 3i-l show an increased concentration in the bottom part of the enclosure. It is also noticed that Figs. 3j and 3k slightly differ from each other because the water distribution is not uniform in the thickness direction.

Additionally, it is also observed that there exists about 3mm difference between the ground truth and the image in Z-direction as shown in Fig. 3a, which is due to the device delay. In addition, Figs. 3e and 3i also recover the front and back boundaries at Z = 118mm and Z = 124mm, which proves that 3mm's delay is constant for different scans. Furthermore, the distance between two boundaries is just 6mm, smaller than thickness of the sand cell. There are two factors contributing to this result: firstly, the acoustics properties of water-saturated sand are assumed to be unknown during the image reconstruction, and the properties of oil are used instead; secondly, the thickness of marker enclosure is smaller than the thickness of sand cell, which is about 6.5mm. Despite these precision tolerances, our TA imaging accurately recovers the shape of the water distribution in the testbed.

## 5 Conclusions

In this letter, we have demonstrated that thermoacoustic pressure waves, which result from the thermodynamic coupling of electromagnetic and mechanical waves, can be used for detecting and discerning water saturation in the subsurface. Moreover, the relationship between the amplitude of the thermoacustic pressure wave and the water saturation level is strictly monotonic, as predicted by our computational simulation and validated by the experimental data. On the basis of this result, we conducted a second experiment that demonstrated the feasibility of using thermoacustic waves to reconstruct fluid distribution in a quasi-3D sand cell. The superficial water saturation levels inferred from the optical ground truth images are in good agreement with the images reconstructed with our thermoacustic data. Both optical and thermoacustic images reveal the intrinsic effect of gravity on the distribution of the fluid on the porous media; however thermoacoustic imaging have the ability to do so quantitatively and in 3D. For the sake of reliability and simplicity in this first demonstration, only one mechanically scanned transducer was used to collect the TA data; a choice that limits the scanning speed and does not have the temporal resolution necessary to track the dynamic gravity-driven fluid motion. Ongoing efforts in our lab are currently geared towards performing real-time imaging of fluid flow in porous media by using arrays of receiving transducers and volumetric coding fused with compressive imaging.

## Open Research

The imaging algorithm is introduced in the supplementary file, and the experiment data is available on the Zenodo platform via https://doi.org/10.5281/zenodo.7465796.


## Acknowledgments

This work has been partially funded by the Department of Energy (Award DE-SC0017614) and the NSF CAREER program (Award No. 1653671). RL was partly supported by the Abdul Latif Jameel World Water and Food Security Lab (J-WAFS) at MIT. RJ acknowledges funding from the US Department of Energy (Award DE-SC0018357).


## References


Berg, S., Ott, H., Klapp, S. A., Schwing, A., Neiteler, R., Brussee, N., ... others (2013). Real-time 3D imaging of Haines jumps in porous media flow. *Proceedings of the National Academy of Sciences*, *110*(10), 3755–3759.

Beven, K., & Germann, P. (1982). Macropores and water flow in soils. *Water Resour. Res.*, *18*(5), 1311–1325.

Beven, K., & Germann, P. (2013). Macropores and water flow in soils revisited. *Water Resources Research*, *49*(6), 3071–3092.

Blunt, M. J., Bijeljic, B., Dong, H., Gharbi, O., Iglauer, S., Mostaghimi, P., ... Pentland, C. (2013). Pore-scale imaging and modelling. *Advances in Water resources*, *51*, 197–216.

Cnudde, V., & Boone, M. N. (2013). High-resolution x-ray computed tomography in geosciences: A review of the current technology and applications. *Earth-Science Reviews*, *123*, 1–17.

Cui, Y., Yuan, C., & Ji, Z. (2017). A review of microwave-induced thermoacoustic imaging: Excitation source, data acquisition system and biomedical applications. *Journal of Innovative Optical Health Sciences*, *10*(04), 1730007.

Dalbe, M. J., & Juanes, R. (2018). Morphodynamics of fluid–fluid displacement in 3d deformable granular media. *Phys. Rev. Applied*, *9*, 024028.

David, C., Barnes, C., Desrues, M., Pimienta, L., Sarout, J., & Dautriat, J. (2017). Ultrasonic monitoring of spontaneous imbibition experiments: Acoustic signature of fluid migration. *Journal of Geophysical Research: Solid Earth*, *122*(7), 4931–4947.

David, C., Bertauld, D., Dautriat, J., Sarout, J., Menéndez, B., & Nabawy, B. (2015). Detection of moving capillary front in porous rocks using x-ray and ultrasonic methods. *Frontiers in Physics*, *3*, 53.

Glass, R. J., Parlange, J.-Y., & Steenhuis, T. S. (1989). Wetting front instability, 2. Experimental determination of relationships between system parameters and two-dimensional unstable flow field behaviour in initially dry porous media. *Water Resour. Res.*, *25*(6), 1195–1207.

Heredia-Juesas, J., Molaei, A., Tirado, L., & Martínez-Lorenzo, J. Á. (2021). Consensus and sectioning-based admm with norm-1 regularization for imaging with a compressive reflector antenna. *IEEE Transactions on Computational Imaging*, *7*, 1189–1204.

Inc., C. (2020). *Comsol* [software]. v5.2. Retrieved from `http://www.comsol.com/products/multiphysics/`

Jarvis, N. (2007). A review of non-equilibrium water flow and solute transport in soil macropores: Principles, controlling factors and consequences for water quality. *European Journal of Soil Science*, *58*(3), 523–546.

Jarvis, N., Koestel, J., & Larsbo, M. (2016). Understanding preferential flow in the vadose zone: Recent advances and future prospects. *Vadose Zone Journal*, *15*(12), 1–11.

Katuwal, S., Hermansen, C., Knadel, M., Moldrup, P., Greve, M. H., & de Jonge, L. (2018). Combining x-ray computed tomography and visible near-infrared spectroscopy for prediction of soil structural properties. *Vadose Zone Journal*, *17*(1), 160054.

Koestel, J., & Larsbo, M. (2014). Imaging and quantification of preferential solute transport in soil macropores. *Water Resources Research*, *50*(5), 4357–4378.

Kong, X.-Z., Holzner, M., Stauffer, F., & Kinzelbach, W. (2011). Time-resolved 3D visualization of air injection in a liquid-saturated refractive-index-matched porous medium. *Exp. Fluids*, *50*(6), 1659–1670.

Krummel, A. T., Datta, S. S., Münster, S., & Weitz, D. A. (2013). Visualizing multiphase flow and trapped fluid configurations in a model three-dimensional porous medium. *AIChE J.*, *59*(3), 1022–1029.

Liu, C., Ghanbarzadeh-Dagheyan, A., Heredia-Juesas, J., Molaei, A., & Martinez-Lorenzo, J. A. (2018). The study of holey cavity in the application of thermoacoustics imaging. In *ASME International Mechanical Engineering Congress and Exposition* (Vol. 52163, p. V011T01A025).

Liu, C., Mao, X., Heredia Juesas, J., Molaei, A., & Martinez-Lorenzo, J. A. (2019). Preliminary results of microwave induced thermoacoustics imaging in geological media. In *ASME International Mechanical Engineering Congress and Exposition* (Vol. 59483, p. V011T01A017).

Liyanage, R., Cen, J., Krevor, S., Crawshaw, J. P., & Pini, R. (2019). Multidimensional observations of dissolution-driven convection in simple porous media using x-ray ct scanning. *Transp. Porous Media*, *126*(2), 355–378.

Liyanage, R., & Juanes, R. (2021). *Electronic data repository for 'Gravity fingering control on evaporation and deep drainage in a 3D porous medium'.* URL: https://doi.org/10.5281/zenodo.4425884.

Lorenzo, J. A. M., Juesas, J. H., & Blackwell, W. (2015). A single-transceiver compressive reflector antenna for high-sensing-capacity imaging. *IEEE Antennas and Wireless Propagation Letters*, *15*, 968–971.

Lou, C., Yang, S., Ji, Z., Chen, Q., & Xing, D. (2012). Ultrashort microwave-induced thermoacoustic imaging: a breakthrough in excitation efficiency and spatial resolution. *Physical review letters*, *109*(21), 218101.

Luo, L., Lin, H., & Halleck, P. (2008). Quantifying soil structure and preferential flow in intact soil using x-ray computed tomography. *Soil Science Society of America Journal*, *72*(4), 1058–1069.

Mao, X., Liu, C., Heredia-Juesas, J., & Martinez-Lorenzo, J. A. (2020). Microwave-induced thermoacoustic compressive imaging with metamaterial coding. In *Asme international mechanical engineering congress and exposition* (Vol. 84478, p. V001T01A018).

Moebius, F., & Or, D. (2012). Interfacial jumps and pressure bursts during fluid displacement in interacting irregular capillaries. *Journal of colloid and interface science*, *377*(1), 406–415.

Müller, S., Niederleithinger, E., & Bohlen, T. (2012). Reverse time migration: A seismic imaging technique applied to synthetic ultrasonic data. *International Journal of Geophysics*, *2012*, 128465.

Pimienta, L., David, C., Sarout, J., Perrot, X., Dautriat, J., & Barnes, C. (2019). Evolution in seismic properties during low and intermediate water saturation: Competing mechanisms during water imbibition? *Geophysical Research Letters*, *46*(9), 4581–4590.

Pohlmeier, A., Garré, S., & Roose, T. (2018). Noninvasive imaging of processes in natural porous media: From pore to field scale. *Vadose zone journal*, *17*(1), 1–3.

Richter, D. d., & Mobley, M. L. (2009). Monitoring Earth's critical zone. *Science*, *326*, 1067–1068.

Roman, S., Soulaine, C., & Kovscek, A. R. (2020). Pore-scale visualization and characterization of viscous dissipation in porous media. *Journal of Colloid and Interface Science*, *558*, 269–279.

Sharma, P., Aswathi, P., Sane, A., Ghosh, S., & Bhattacharya, S. (2011). Three-dimensional real-time imaging of bi-phasic flow through porous media. *Rev. Sci. Instrum.*, *82*, 113704.

Shen, L., Savre, W., Price, J., & Athavale, K. (1985). Dielectric properties of reservoir rocks at ultra-high frequencies. *Geophysics*, *50*(4), 692–704.

Troschke, B., & Burkhardt, H. (1998). Thermal conductivity models for two-phase systems. *Physics and Chemistry of the Earth*, *23*(3), 351–355.

Waples, D. W., & Waples, J. S. (2004). A review and evaluation of specific heat capacities of rocks, minerals, and subsurface fluids. part 1: Minerals and nonporous rocks. *Natural resources research*, *13*(2), 97–122.

Wei, Y., Cejas, C. M., Barrois, R., Dreyfus, R., & Durian, D. J. (2014). Morphology of rain water channeling in systematically varied model sandy soils. *Phys. Rev. Applied*, *2*, 044004.

Werth, C. J., Zhang, C., Brusseau, M. L., Oostrom, M., & Baumann, T. (2010). A review of non-invasive imaging methods and applications in contaminant hydrogeology research. *Journal of Contaminant Hydrology*, *113*(1-4), 1–24.

Wildenschild, D., Vaz, C., Rivers, M., Rikard, D., & Christensen, B. (2002). Using x-ray computed tomography in hydrology: systems, resolutions, and limitations. *Journal of Hydrology*, *267*(3-4), 285–297.

Xu, M., & Wang, L. V. (2006). Photoacoustic imaging in biomedicine. *Review of scientific instruments*, *77*(4), 041101.

Yin, B., Xing, D., Wang, Y., Zeng, Y., Tan, Y., & Chen, Q. (2004). Fast photoacoustic imaging system based on 320-element linear transducer array. *Physics in Medicine & Biology*, *49*(7), 1339.

Zhang, Y., Zhang, Z., Ma, Z., Chen, J., Akbar, J., Zhang, S., ... Cerdà, A. (2018). A review of preferential water flow in soil science. *Canadian Journal of Soil Science*, *98*(4), 604–618.

Zou, X., Song, H., Wang, C., & Ma, Z. (2016). Relationships between b-mode ultrasound imaging signals and suspended sediment concentrations. *Measurement*, *92*, 34–41.

Zou, X., Wang, C., Song, H., Han, Z., Ma, Z., & Hu, W. (2018). Applications of ultrasound imaging system for measuring water-sand parameters during sediment transport process in hydraulic model experiments. *Journal of Hydroinformatics*, *20*(2), 410–423.

# Monitoring Preferential Flow of Water in Sand Using Thermoacoustics Wave Imaging

**Chang Liu [1], Xu Mao [1], Chang Wang [1], Rebecca Liyanage [2], Juan Heredia Juesas [1,3], Ruben Juanes [2], Jose Angle Martinez-Lorenzo [1,3]**

[1]Department of Mechanical and Industrial Engineering, Northeastern University, Boston, Massachusetts, 02115
[2]Department of Civil and Environmental Engineering, Massachusetts Institute of Technology, Cambridge, Massachusetts, 02139
[3]Department of Electrical and Computer Engineering, Northeastern University, Boston, Massachusetts, 02115

**Key Points:**

- The relationship between water saturation in sand and the resultant thermoacoustics wave amplitude is monotonic.
- The reconstructed thermoacoustics images match well with the optical ground truth for water-saturated sand.
- Thermoacoustics imaging enables real-time monitoring of water distribution in subsurface sand.

Corresponding author: Chang Liu, liu.chang4@northeastern.edu

Corresponding author: Jose Angel Martinez-Lorenzo, j.martinez-lorenzo@northeastern.edu

**Abstract**

Accurate predictions of fluid flow, mass transport, and reaction rates critically impact the efficiency and reliability of subsurface exploration and sustainable use of subsurface resources. Quantitative dynamical sensing and imaging can play a pivotal role in the ability to make such predictions. Geophysical thermoacoustic technology has the potential to provide the aforementioned capabilities, since it builds upon the principle that electromagnetic and mechanical wave fields can be coupled through a thermodynamic process. In this letter, we present laboratory experiments featuring the efficacy of thermoacustic imaging in the monitoring of preferential flow of water in porous media. Our laboratory experimental equipment can be readily packaged in a form factor that fits in a borehole, and the use of multiple acoustic transducers—which can be combined with volumetric coding techniques—has the potential to provide quasi-real-time imaging (0.5 Hertz video rate) of regions in close proximity (a few meters) of an open field well.


## Plain Language Summary

Multiphysics subsurface sensing and imaging technology has the potential to provide unique insights to better understand multiphase flow and transport in porous media in 4D (time and space). Conventional high-resolution, laboratory-based imaging technology—such as X-ray or MRI—require power-hungry and often bulky equipment; the latter limits their use in open field experiments and challenges their ability to perform real-time image reconstruction. Acoustics Doppler imaging has been used for real-time flow velocity monitoring in biomedical applications; however, the relationship between fluid saturation in porous media and measured acoustic pressure still requires further investigation. In this letter we show how microwave-induced thermoacoustic (TA) imaging technology can be applied to monitor water distribution in sand. In contrast to traditional acoustic imaging, the proposed TA method exhibits a dominant monotonic relationship between the degree of water saturation and the measured amplitude of the TA pressure. Our experimental results show the efficacy of TA technology for imaging 2D water distribution profiles in sand. The reconstructed TA images are in good agreement with the optical ground truth water distribution map, thus illustrating the feasibility of the proposed method for real-world field applications in agricultural and hydrological sciences.

## 1 Introduction

Understanding the distribution of fluid phases during multiphase flow in porous media is critical in a wide array of subsurface natural processes and engineering applications (Jarvis, 2007; Blunt et al., 2013; Berg et al., 2013). Optical imaging, X-ray tomography, and magnetic resonance imaging (MRI) are just a few of the most commonly used non-invasive, high-resolution imaging techniques (Katuwal et al., 2018; Pohlmeier et al., 2018; Cnudde & Boone, 2013). However, these methods are subject to important drawbacks that not only limit their use in field applications but also in controlled laboratory environments (Werth et al., 2010; Wildenschild et al., 2002). Optical imaging techniques are well suited to reconstruct fluid distribution in a real-time fashion; however, their use is mostly limited to 2D geometries due reduced penetration on light in highly opaque media and fluid saturation cannot be easily quantified (Moebius & Or, 2012; Roman et al., 2020), although advances such as refraction-index matching, planar laser-induced fluorescence and confocal microscopy have extended the range of application of 3D optical (Kong et al., 2011; Sharma et al., 2011; Krummel et al., 2013; Dalbe & Juanes, 2018). In contrast, X-ray and MRI methods can provide a quantified high-resolution image of 3D geometries (Pohlmeier et al., 2018; Liyanage et al., 2019); however, these methods are limited in their ability to capture the transient behavior of fast fluid flow due to its intrinsic slow scanning speed (Luo et al., 2008; Koestel & Larsbo, 2014). For example, preferential flow, which refers to the phenomenon of channeling in-filtrating water as a result of 'macropores' (Beven & Germann, 1982) or gravitational instability (Glass et al., 1989; Wei et al., 2014; Liyanage & Juanes, 2021), can reach a wetting front velocity up several millimeters per second, calling for a real-time imaging method in 3D (Zhang et al., 2018; Jarvis et al., 2016; Beven & Germann, 2013).

Acoustic (AC) and seismic waves are commonly used for subsurface situational awareness (Müller et al., 2012; David et al., 2015); however, the intrinsic relationship between acoustic properties of rocks and fluid saturation remains poorly understood. Nevertheless, it has been shown that an increase in water saturation modulates the amplitude of P-waves, which ultimately gives form to the acoustics signature of heterogeneous mixtures of rocks and fluids (Pimienta et al., 2019; David et al., 2017). While ultrasound imaging has been applied in geophysics, the vague relationship between the morphology of the sample under test and ultrasound image suggests that further advances are needed before this methodology can be used in quantitative dynamical imaging applications (Zou et al., 2016, 2018).

TA sensing and imaging presents a new opportunity to better characterize the subsurface due to its inherent multiphysics nature, in which elastic waves are created due to the thermal expansion and contraction of a target when it is illuminated by a high intensity microwave source (Liu et al., 2018). This technology, originally used for breast cancer detection, leverages on the high contrast existing between healthy and cancerous tissues at microwaves frequencies and the high resolution of AC technology to create images with a pixel resolution of tens of micrometers (Lou et al., 2012). Such a thermodynamics-driven coupling of electromagnetic and mechanical waves overcomes the intrinsic poor resolution of electromagnetic images and the low contrast of AC images when used in a standalone fashion (Cui et al., 2017; Xu & Wang, 2006). At particular spatial scales, there are certain similarities amongst the constitutive properties of biological and geological materials—suggesting that TA technology may be used for geophysical imaging applications. The latter assumption was experimentally tested and validated in (Liu et al., 2019); the authors demonstrated that geological materials, such as sand and rocks, can indeed generate detectable TA pressure waves. Moreover, the significant contrast existing between the dielectric constants of water and quartz sand enables the monitoring of fluid distribution in sandy environments.

Conventional real-time imaging systems use arrays of transducers, often involving over 100 receivers, to collect large amounts of information in a reduced amount of time; however, these bulky, power-hungry, and often expensive devices constrain the use of TA imaging in open field scenarios (Yin et al., 2004). TA technology is well poised to enable real-time imaging while using a reduced number of receivers. The latter is afforded by performing volumetric spatial coding of the wave fields (Lorenzo et al., 2015) to maximize the sensing capacity of the imaging system, which is defined as the information-transfer efficiency between imaging domain and the measured data. Volumetric coding can be performed using artificial metamaterials, holey cavities, and compressive reflectors; this reduces the mutual information among successive measurements and increase the sensing capacity of the imaging system (Mao et al., 2020).

In this letter we present the first study showing the efficacy of microwave-induced thermoacoustics imaging to monitor fluid distribution in geological media. This technique has the potential to offer real-time reconstruction of fluid flow in 4D, at distance, and using non-contact sensors—an ability that could prove instrumental to extend our understanding of water distribution and heterogeneous infiltration in the Earth's critical zone (Richter & Mobley, 2009). This letter is structured as follows: In Section 2 we introduce the background theory of applying TA waves to monitor water distribution in sand. Based on this, we establish a simulation model to predict the relationship between water saturation and the TA signal strength. We design an experiment to validate this principle. In Section 3, we analyze the data from the simulation and experiment, both showing a monotonic relationship between water saturation and TA signal amplitude.

Table 1: Material properties used in simulation

| Material | $\epsilon_r$ | $\sigma$ [S/m] | $\rho$ [kg/m$^3$] | $\kappa$ [GPa] | $\beta$ [$10^{-6}$/K] | $C_p$ [J/(kg· K)] |
|---|---|---|---|---|---|---|
| Quartz Sand | 4.27 | 0 | 2650 | 37 | 1 | 743 |
| Water | 80 | 0.05 | 1000 | 2.25 | 210 | 4180 |
| Air | 1 | 0 | - | - | - | - |
| Oil | 2.6 | 0.01 | - | - | - | - |
| Acrylic Sheet | 3.4 | $6.7 \times 10^{-15}$ | - | - | - | - |

In Section 4 we present the experimental results of recovering the water distribution profile in a quasi-3D sand cell (in which one dimension is smaller than the other two), and in Section 5 we summarize the main outcomes of our study.

## 2 Materials and Methods

Microwave induced TA pressure waves are generated due to the thermal expansion of an object when it is illuminated by a short, intense microwave pulse. The governing equations for TA wave are:

$$\nabla^2 p(\mathbf{r},t) - \frac{1}{c^2(\mathbf{r})}\frac{\partial^2}{\partial t^2}p(\mathbf{r},t) = -\frac{\beta(\mathbf{r})}{C_p(\mathbf{r})}\frac{\partial Q(\mathbf{r},t)}{\partial t} \tag{1a}$$

$$Q(\mathbf{r},t) \approx \sigma(\mathbf{r})||E(\mathbf{r})||^2 f^2(t) \tag{1b}$$

where $p(\mathbf{r},t)$ is the pressure, $c(\mathbf{r})$ is the sound speed, $\beta(\mathbf{r})$ is the thermal expansion rate, $C_p(\mathbf{r})$ is the heat capacity, and $Q(\mathbf{r},t)$ is the heat source. This term is defined in Eq. (1b), where $\sigma(\mathbf{r})$ is the electric conductivity, $\mathbf{E}(\mathbf{r})$ is the electric field, and $f(t)$ is the excitation pulse function. According to Eq. (1b), the right hand side of Eq. (1a) can be written as $-\frac{\beta(\mathbf{r})}{C_p(\mathbf{r})}\sigma(\mathbf{r})||E(\mathbf{r})||^2\frac{\partial}{\partial t}f^2(t)$. This term can be decomposed as the product of two functions: one is a time varying modulating signal $\frac{\partial}{\partial t}f^2(t)$; and the other is a material-dependent space varying distribution $S(\mathbf{r}) = -\frac{\beta(\mathbf{r})}{C_p(\mathbf{r})}\sigma(\mathbf{r})||E(\mathbf{r})||^2$. The constitutive properties within the source term $S(\mathbf{r})$ are affected by the water saturation of the sandy porous medium, and their value can be approximated by empirical rock physics models (RPMs). The latter provides an estimation of the constitutive properties of the compound mixture and the volume fraction of each one of its individual components.

Our first experiment is aimed at the computational modeling and experimental testing of the effect of water saturation on the signal strength. A multiphysics engine (Inc., 2020) was used to reveal such relationship. Figure 1a displays the baseline geometry of the simulation; the material properties are predicted using the RPMs described in (Shen et al., 1985; Troschke & Burkhardt, 1998; Waples & Waples, 2004) and summarized in Table 1—where $\epsilon_r$ is the relative permittivity, $\rho$ is the density, and $\kappa$ is the bulk modulus. TA pressure signals as well as the source strength predicted by the computational models are contrasted with those experimentally measured in the first of our TA imaging testbeds. Six sand samples having different quantitatively-controlled saturation levels are prepared for the experiment.

The second experiment is aimed at demonstrating that TA imaging can effectively be used to monitor fingered water infiltration in a quasi-3D sand cell. The testbed is shown in Fig. 1c. Since only one transducer is applied in the experiment, the sand cell with static water distribution is imaged.

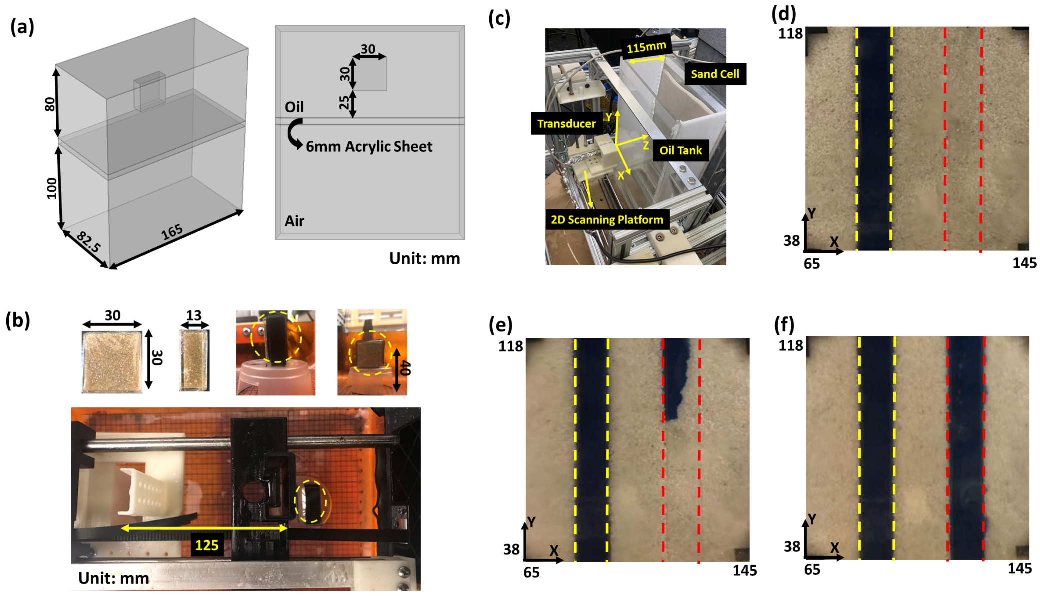


Figure 1: Monitoring water distribution profile in sand using the TA wave: (a) RPM-driven simulation geometry, (b) the testbed for the first experiment, (c) the testbed for the second experiment, (d) water distribution inside the marker, (e) water distribution after the first injection, and (f) water distribution after the second injection.

## 3 Data Collection

In the first experiment, a plastic box with one facet removed is filled with 12.5g of sand (#20 graded). The size of the sand box is 30mm×30mm×13mm, as shown in Fig. 1b. While keeping the dry sample for comparison, the other five samples are injected with different amounts of water: 0.7g, 1.4g, 2.1g, 2.8g, and 3.5g, separately. Provided that the porosity of sand sample is $\Phi = 30\%$, this results in water saturations of 20%, 40%, 60%, 80%, and 100% for each sample, respectively. Later, the sand box is sealed with a thin layer of plastic wrap and black waterproof tape. Finally, the sand box is held still for 1 hour to allow for the water to spread through the sample, since the water is injected from the opening facet of the sample. As it can be seen in Fig. 1b, the sand sample is placed parallel to the transducer in the oil bath at a distance of 125mm away from the transducer. Moreover, the center of the sand sample is lifted 40mm to match the height of the transducer. After one measurement is finished, the previous sand box is replaced with another sand sample with different saturation level.

In the second experiment, the quasi-3D sand cell (10mm thickness) is separated from the acoustic transducer by an oil tank. The distance between the sand cell and the transducer is 115mm. The sand sample under test is geometrically constrained to a small narrow region using a plastic enclosure, and two such enclosures are prepared: the left one is fully saturated as the marker for reference (yellow dashed line in Fig. 1d), and the right one is for dynamic water distribution imaging (red dashed line in Fig. 1d). In the first part of this experiment, 1.5mL of blue-dyed water is injected from the top into the right enclosure, which is shown in Fig. 1e. In the second part of this experiment, additional amount of 3.9mL of blue-dyed water is injected into the right enclosure, and the final water distribution is shown in Fig. 1f. In this experiment, the selected imaging area ranges from X = 65mm to X = 145mm, Y = 38mm to Y = 118mm, and Z = 100mm to Z = 140mm. The scanning range of transducer is slightly larger than the imaging area to achieve

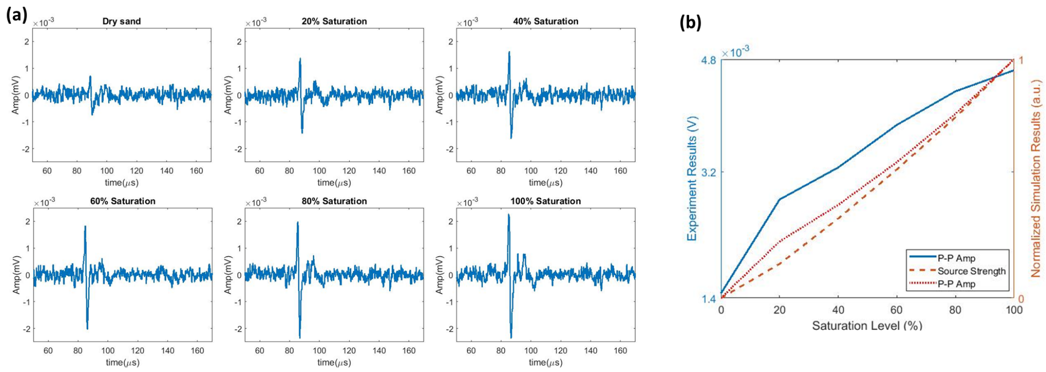


Figure 2: The monotonic relationship between water saturation and the TA amplitude: (a) measured signals of the sand box saturated by different amount of water, and (b) the peak-peak amplitude of the collected signals (solid line), the simulated source strength (dashed line) and the peak-peak amplitude (dotted line) after normalization.

better resolution in X-Y plane, ranging from X = 53mm to X = 157mm in X-direction and Y = 26mm to Y = 130mm in Y-direction. The raster scan is conducted four times: dry sand, after the preparation of the marker, after the first injection and after the second injection into the right enclosure. Moreover, to guarantee the fully spread of water, the raster scan starts after the water profile stops moving. The measurements are collected with 4mm spatial separation for every measured point, thus making a total number of 729 measurements for each scan. During these scans, the power of the EM wave remains constant, and the difference between the successive measurements should be the effect of the injected water.

## 4 Results

In the first experiment, the collected TA signals for samples with different water saturations are plotted in Fig. 2a. As it can be seen, the amplitudes of the measured signals depend on the amount of water in the sand. The peak-peak value of those signals are plotted in Fig. 2b, and the simulated source strengths as well as the peak-peak amplitudes are also shown for comparison after normalization. Several points in Fig. 2b deserve discussion. All results in Fig. 2b exhibit a strictly monotonic relationship between the TA signal amplitude with the amount of injected water, which reveals the feasibility of distinguishing the water saturation in sand using TA waves. The simulated results of peak-peak amplitude and source strength both show a nearly linear relationship against the saturation level, which can be used as a prediction for the water saturation level in the following experiment. We also observe that the dry sand can transmit a detectable TA wave in the experiment while the simulation result shows a zero source strength. This is because the sand used in the experiment is not fully dehydrated. Furthermore, the trend of the experimental measurements exhibit a reversed curvature when compared to that of the simulated results, which may be attributed to by several factors. Firstly, the numerical simulation considers the sample to have a homogeneous distribution of water saturation; while the experiment may have a heterogeneous one due to the water injection in the open facet of the box. Secondly, there may exist important differences between the material properties predicted by the selected RPM and the sand sample used in the experiment.

In the second experiment, the left enclosure, as shown in Fig. 1d, is fully saturated to determine the saturation level of the dynamic water distribution inside the right en-

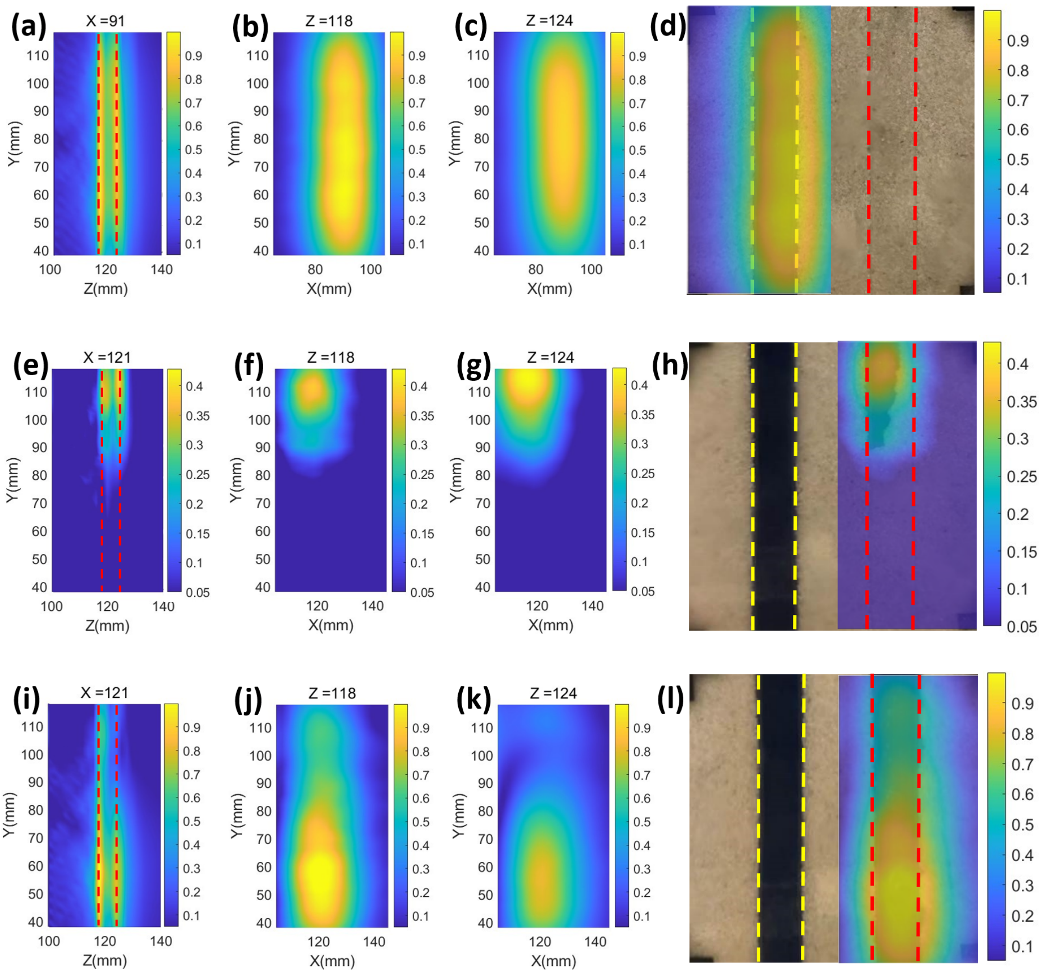


Figure 3: Water distribution reconstruction using the TA waves: (a) slice taken at X = 91mm for marker, (b) slice taken at Z = 118mm for marker, (c) slice taken at Z = 124mm for marker, (d) overlapping marker image with ground truth, (e) slice taken at X = 121mm for the first injection, (f) slice taken at Z = 118mm for the first injection, (g) slice taken at Z = 124mm for the first injection, (h) overlapping the first injection image with ground truth, (i) slice taken at X = 121mm for the second injection, (j) slice taken at Z = 118mm for the second injection, (k) slice taken at Z = 124mm for the second injection, and (l) overlapping the second injection image with ground truth.

closure based on the simulated results presented in the first experiment. The images after first infiltration—Fig. 1e—show that the color intensity of the fluid map is mainly remained on the top. Moreover, the fluid distribution after the second injection has spread to the whole area of the enclosure compared with the first injection. This visual information is used as optical ground truth to drive the comparison with the TA image.

Figure 3a presents the imaging result of a cross section (X = 91mm) for the marker area, which shows the capability of TA imaging to recover subsurface information of the sandy medium. It is noteworthy that the position of the selected cross section is not at the center of the imaging area but, rather, at the center of the marker area. As shown in Fig. 3a, the intensity of the image stays constant from top to the bottom of the enclosure, in agreement with the optical ground truth of Fig. 1d. Furthermore, the first peak appears at Z = 118mm and the second peak appears at Z = 124mm in the image, corresponding to the front and back boundary of the sand cell, individually. In addition, the image strength at the first and second peaks is similar because the EM wave is transmitted from the back (negative X direction), which partly compensates for the attenuation effect. The reconstructed images of the water infiltration profile in the X-Y plane are shown in Figs. 3b and 3c, which correspond to the slice taken at Z = 118mm and Z = 124mm, respectively. Both recovered images show an uniform distribution inside the area of the enclosure. Figure 3d overlaps the ground truth of marker with the front boundary image. Figures 3e-h present the imaging results after the first injection. In contrast with Fig. 3a, the image strength in Fig. 3e stays on the top part of the enclosure, which agrees with the ground truth in Fig. 3h. Compared with those results of the first injection, the recovered images for the second injection in Figs. 3i-l show an increased concentration in the bottom part of the enclosure. It is also noticed that Figs. 3j and 3k slightly differ from each other because the water distribution is not uniform in the thickness direction.

Additionally, it is also observed that there exists about 3mm difference between the ground truth and the image in Z-direction as shown in Fig. 3a, which is due to the device delay. In addition, Figs. 3e and 3i also recover the front and back boundaries at Z = 118mm and Z = 124mm, which proves that 3mm's delay is constant for different scans. Furthermore, the distance between two boundaries is just 6mm, smaller than thickness of the sand cell. There are two factors contributing to this result: firstly, the acoustics properties of water-saturated sand are assumed to be unknown during the image reconstruction, and the properties of oil are used instead; secondly, the thickness of marker enclosure is smaller than the thickness of sand cell, which is about 6.5mm. Despite these precision tolerances, our TA imaging accurately recovers the shape of the water distribution in the testbed.

## 5 Conclusions

In this letter, we have demonstrated that thermoacoustic pressure waves, which result from the thermodynamic coupling of electromagnetic and mechanical waves, can be used for detecting and discerning water saturation in the subsurface. Moreover, the relationship between the amplitude of the thermoacustic pressure wave and the water saturation level is strictly monotonic, as predicted by our computational simulation and validated by the experimental data. On the basis of this result, we conducted a second experiment that demonstrated the feasibility of using thermoacustic waves to reconstruct fluid distribution in a quasi-3D sand cell. The superficial water saturation levels inferred from the optical ground truth images are in good agreement with the images reconstructed with our thermoacustic data. Both optical and thermoacustic images reveal the intrinsic effect of gravity on the distribution of the fluid on the porous media; however thermoacoustic imaging have the ability to do so quantitatively and in 3D. For the sake of reliability and simplicity in this first demonstration, only one mechanically scanned transducer was used to collect the TA data; a choice that limits the scanning speed and does not have the temporal resolution necessary to track the dynamic gravity-driven fluid motion. Ongoing efforts in our lab are currently geared towards performing real-time imaging of fluid flow in porous media by using arrays of receiving transducers and volumetric coding fused with compressive imaging.

## Open Research

The imaging algorithm is introduced in the supplementary file, and the experiment data is available on the Zenodo platform via https://doi.org/10.5281/zenodo.7465796.

## Acknowledgments

This work has been partially funded by the Department of Energy (Award DE-SC0017614) and the NSF CAREER program (Award No. 1653671). RL was partly supported by the Abdul Latif Jameel World Water and Food Security Lab (J-WAFS) at MIT. RJ acknowledges funding from the US Department of Energy (Award DE-SC0018357).

## References

Berg, S., Ott, H., Klapp, S. A., Schwing, A., Neiteler, R., Brussee, N., ... others (2013). Real-time 3D imaging of Haines jumps in porous media flow. *Proceedings of the National Academy of Sciences*, *110*(10), 3755–3759.

Beven, K., & Germann, P. (1982). Macropores and water flow in soils. *Water Resour. Res.*, *18*(5), 1311–1325.

Beven, K., & Germann, P. (2013). Macropores and water flow in soils revisited. *Water Resources Research*, *49*(6), 3071–3092.

Blunt, M. J., Bijeljic, B., Dong, H., Gharbi, O., Iglauer, S., Mostaghimi, P., ... Pentland, C. (2013). Pore-scale imaging and modelling. *Advances in Water resources*, *51*, 197–216.

Cnudde, V., & Boone, M. N. (2013). High-resolution x-ray computed tomography in geosciences: A review of the current technology and applications. *Earth-Science Reviews*, *123*, 1–17.

Cui, Y., Yuan, C., & Ji, Z. (2017). A review of microwave-induced thermoacoustic imaging: Excitation source, data acquisition system and biomedical applications. *Journal of Innovative Optical Health Sciences*, *10*(04), 1730007.

Dalbe, M. J., & Juanes, R. (2018). Morphodynamics of fluid–fluid displacement in 3d deformable granular media. *Phys. Rev. Applied*, *9*, 024028.

David, C., Barnes, C., Desrues, M., Pimienta, L., Sarout, J., & Dautriat, J. (2017). Ultrasonic monitoring of spontaneous imbibition experiments: Acoustic signature of fluid migration. *Journal of Geophysical Research: Solid Earth*, *122*(7), 4931–4947.

David, C., Bertauld, D., Dautriat, J., Sarout, J., Menéndez, B., & Nabawy, B. (2015). Detection of moving capillary front in porous rocks using x-ray and ultrasonic methods. *Frontiers in Physics*, *3*, 53.

Glass, R. J., Parlange, J.-Y., & Steenhuis, T. S. (1989). Wetting front instability, 2. Experimental determination of relationships between system parameters and two-dimensional unstable flow field behaviour in initially dry porous media. *Water Resour. Res.*, *25*(6), 1195–1207.

Heredia-Juesas, J., Molaei, A., Tirado, L., & Martínez-Lorenzo, J. Á. (2021). Consensus and sectioning-based admm with norm-1 regularization for imaging with a compressive reflector antenna. *IEEE Transactions on Computational Imaging*, *7*, 1189–1204.

Inc., C. (2020). *Comsol* [software]. v5.2. Retrieved from `http://www.comsol.com/products/multiphysics/`

Jarvis, N. (2007). A review of non-equilibrium water flow and solute transport in soil macropores: Principles, controlling factors and consequences for water quality. *European Journal of Soil Science*, *58*(3), 523–546.

Jarvis, N., Koestel, J., & Larsbo, M. (2016). Understanding preferential flow in the vadose zone: Recent advances and future prospects. *Vadose Zone Journal*, *15*(12), 1–11.

Katuwal, S., Hermansen, C., Knadel, M., Moldrup, P., Greve, M. H., & de Jonge, L. (2018). Combining x-ray computed tomography and visible near-infrared spectroscopy for prediction of soil structural properties. *Vadose Zone Journal*, *17*(1), 160054.

Koestel, J., & Larsbo, M. (2014). Imaging and quantification of preferential solute transport in soil macropores. *Water Resources Research*, *50*(5), 4357–4378.

Kong, X.-Z., Holzner, M., Stauffer, F., & Kinzelbach, W. (2011). Time-resolved 3D visualization of air injection in a liquid-saturated refractive-index-matched porous medium. *Exp. Fluids*, *50*(6), 1659–1670.

Krummel, A. T., Datta, S. S., Münster, S., & Weitz, D. A. (2013). Visualizing multiphase flow and trapped fluid configurations in a model three-dimensional porous medium. *AIChE J.*, *59*(3), 1022–1029.

Liu, C., Ghanbarzadeh-Dagheyan, A., Heredia-Juesas, J., Molaei, A., & Martinez-Lorenzo, J. A. (2018). The study of holey cavity in the application of thermoacoustics imaging. In *ASME International Mechanical Engineering Congress and Exposition* (Vol. 52163, p. V011T01A025).

Liu, C., Mao, X., Heredia Juesas, J., Molaei, A., & Martinez-Lorenzo, J. A. (2019). Preliminary results of microwave induced thermoacoustics imaging in geological media. In *ASME International Mechanical Engineering Congress and Exposition* (Vol. 59483, p. V011T01A017).

Liyanage, R., Cen, J., Krevor, S., Crawshaw, J. P., & Pini, R. (2019). Multidimensional observations of dissolution-driven convection in simple porous media using x-ray ct scanning. *Transp. Porous Media*, *126*(2), 355–378.

Liyanage, R., & Juanes, R. (2021). *Electronic data repository for 'Gravity fingering control on evaporation and deep drainage in a 3D porous medium'.* URL: https://doi.org/10.5281/zenodo.4425884.

Lorenzo, J. A. M., Juesas, J. H., & Blackwell, W. (2015). A single-transceiver compressive reflector antenna for high-sensing-capacity imaging. *IEEE Antennas and Wireless Propagation Letters*, *15*, 968–971.

Lou, C., Yang, S., Ji, Z., Chen, Q., & Xing, D. (2012). Ultrashort microwave-induced thermoacoustic imaging: a breakthrough in excitation efficiency and spatial resolution. *Physical review letters*, *109*(21), 218101.

Luo, L., Lin, H., & Halleck, P. (2008). Quantifying soil structure and preferential flow in intact soil using x-ray computed tomography. *Soil Science Society of America Journal*, *72*(4), 1058–1069.

Mao, X., Liu, C., Heredia-Juesas, J., & Martinez-Lorenzo, J. A. (2020). Microwave-induced thermoacoustic compressive imaging with metamaterial coding. In *Asme international mechanical engineering congress and exposition* (Vol. 84478, p. V001T01A018).

Moebius, F., & Or, D. (2012). Interfacial jumps and pressure bursts during fluid displacement in interacting irregular capillaries. *Journal of colloid and interface science*, *377*(1), 406–415.

Müller, S., Niederleithinger, E., & Bohlen, T. (2012). Reverse time migration: A seismic imaging technique applied to synthetic ultrasonic data. *International Journal of Geophysics*, *2012*, 128465.

Pimienta, L., David, C., Sarout, J., Perrot, X., Dautriat, J., & Barnes, C. (2019). Evolution in seismic properties during low and intermediate water saturation: Competing mechanisms during water imbibition? *Geophysical Research Letters*, *46*(9), 4581–4590.

Pohlmeier, A., Garré, S., & Roose, T. (2018). Noninvasive imaging of processes in natural porous media: From pore to field scale. *Vadose zone journal*, *17*(1), 1–3.

Richter, D. d., & Mobley, M. L. (2009). Monitoring Earth's critical zone. *Science*, *326*, 1067–1068.

Roman, S., Soulaine, C., & Kovscek, A. R. (2020). Pore-scale visualization and characterization of viscous dissipation in porous media. *Journal of Colloid and Interface Science*, *558*, 269–279.

Sharma, P., Aswathi, P., Sane, A., Ghosh, S., & Bhattacharya, S. (2011). Three-dimensional real-time imaging of bi-phasic flow through porous media. *Rev. Sci. Instrum.*, *82*, 113704.

Shen, L., Savre, W., Price, J., & Athavale, K. (1985). Dielectric properties of reservoir rocks at ultra-high frequencies. *Geophysics*, *50*(4), 692–704.

Troschke, B., & Burkhardt, H. (1998). Thermal conductivity models for two-phase systems. *Physics and Chemistry of the Earth*, *23*(3), 351–355.

Waples, D. W., & Waples, J. S. (2004). A review and evaluation of specific heat capacities of rocks, minerals, and subsurface fluids. part 1: Minerals and nonporous rocks. *Natural resources research*, *13*(2), 97–122.

Wei, Y., Cejas, C. M., Barrois, R., Dreyfus, R., & Durian, D. J. (2014). Morphology of rain water channeling in systematically varied model sandy soils. *Phys. Rev. Applied*, *2*, 044004.

Werth, C. J., Zhang, C., Brusseau, M. L., Oostrom, M., & Baumann, T. (2010). A review of non-invasive imaging methods and applications in contaminant hydrogeology research. *Journal of Contaminant Hydrology*, *113*(1-4), 1–24.

Wildenschild, D., Vaz, C., Rivers, M., Rikard, D., & Christensen, B. (2002). Using x-ray computed tomography in hydrology: systems, resolutions, and limitations. *Journal of Hydrology*, *267*(3-4), 285–297.

Xu, M., & Wang, L. V. (2006). Photoacoustic imaging in biomedicine. *Review of scientific instruments*, *77*(4), 041101.

Yin, B., Xing, D., Wang, Y., Zeng, Y., Tan, Y., & Chen, Q. (2004). Fast photoacoustic imaging system based on 320-element linear transducer array. *Physics in Medicine & Biology*, *49*(7), 1339.

Zhang, Y., Zhang, Z., Ma, Z., Chen, J., Akbar, J., Zhang, S., … Cerdà, A. (2018). A review of preferential water flow in soil science. *Canadian Journal of Soil Science*, *98*(4), 604–618.

Zou, X., Song, H., Wang, C., & Ma, Z. (2016). Relationships between b-mode ultrasound imaging signals and suspended sediment concentrations. *Measurement*, *92*, 34–41.

Zou, X., Wang, C., Song, H., Han, Z., Ma, Z., & Hu, W. (2018). Applications of ultrasound imaging system for measuring water-sand parameters during sediment transport process in hydraulic model experiments. *Journal of Hydroinformatics*, *20*(2), 410–423.

# Supporting Information for "Monitoring Preferential Flow Distribution in Sand Using Thermoacoustics Wave Imaging Methods"

Chang Liu [1 *], Xu Mao [1], Chang Wang [1], Rebecca Liyanage [2], Juan Heredia Juesas [1,3], Ruben Juanes [2], Jose Angle Martinez-Lorenzo [1,3 †]

[1]Department of Mechanical and Industrial Engineering, Northeastern University, Boston, Massachusetts, 02115

[2]Department of Civil and Environmental Engineering, Massachusetts Institute of Technology, Cambridge, Massachusetts, 02139

[3]Department of Electrical and Computer Engineering, Northeastern University, Boston, Massachusetts, 02115

## Contents of this file

1. Text S1 to S8
2. Figures S1 to S5
3. Table S1

## Additional Supporting Information

1. Caption for Movie S1

---

*liu.chang4@northeastern.edu

†j.martinez-lorenzo@northeastern.edu

**Introduction** This *supplementary materials document* describes our computational simulation model, experimental testbed, data processing pipeline, and imaging algorithm used to generate the results presented in the letter. Moreover, a data repository has been made publicly available to ensure reproducible results. The letter proposes to apply the microwave-induced thermoacoustics imaging (TA) method to reconstruct the water infiltration process in the porous sand. Firstly, a simulation is conducted to establish the relationship between the TA signal strength and the saturation levels. The rock physics model (RPM) used in the simulation is introduced in Text S1, and the simulation model is described in Text S2. Afterward, an experiment is conducted to validate the simulation results. The TA signals generated by sand boxes with different saturation levels are collected in this experiment. The pressure data is converted by the transducer to a voltage signal and collected through an ultrasound receiver at a gain of 79dB. The testbed and experiment process are described in Text S3. Based on the aforementioned results, the finger infiltration experiment can be conducted, and this experiment process is described in Text S4. The data collection system of the finger imaging experiment is similar to that of the sand box experiment. A raster scan is conducted after each experiment stage is finished. The data processing method is described in Text S5, and the imaging algorithm is given in Text S6. It is noticed that the original reconstructed image is in the unit of image strength. However, such information can be used to infer the water saturation level in sand based on the established relationship between the water saturation level and the TA amplitude. This theory is explained in Text S7. Finally, the slow scanning limitations of the current testbed is explained in Text S8.

**Text S1.**

**Rock physics model used for the computational simulations**

A RPM is used to derive the relationship amongst the electromagnetic constitutive properties from rock morphology and fluids distribution in a porous media. The complex dielectric constant $\epsilon_c$ is usually expressed as the combination of relative permittivity $\epsilon_r$ and electric conductivity $\sigma$, as shown in Eq. (1a). The relationship between the porosity $\Phi$ (assuming fully saturated) and the complex dielectric constant $\epsilon_c$ in saturated sand can be modeled by the Bruggerman-Hanna-Sen formula (Shen et al., 1985), which is given in Eq. (1b):

$$\epsilon_c = \epsilon_r - j\frac{\sigma}{\omega_e} \tag{1a}$$

$$\Phi = \frac{\epsilon_c - \epsilon_{c2}}{\epsilon_{c1} - \epsilon_{c_2}(\frac{\epsilon_{c_1}}{\epsilon_c})^{\frac{1}{3}}}, \tag{1b}$$

where $\omega_e$ is the angular frequency of the EM wave, the subscript $[\cdot]_1$ denotes properties of water, $[\cdot]_2$ stands for the properties of dry quartz sand, and $[\cdot]$ for the water-saturated sand. Moreover, the rock physic models of the thermal expansion coefficient $\beta$ (Troschke & Burkhardt, 1998) and specific heat capacity $C_p$ (Waples & Waples, 2004) are given in Eqs. (2a) and (2b), respectively:

$$\beta = \frac{(1-\Phi)\kappa_2\beta_2 + \Phi\kappa_1\beta_1}{(1-\Phi)\kappa_2 + \Phi\kappa_1} \tag{2a}$$

$$C_p = \frac{1}{\rho_2}(\rho_2 C_{p2}(1-\Phi) + \rho_1 C_{p1}\Phi), \tag{2b}$$

where $\kappa$ is the bulk modulus, $\rho$ is the density, and the meanings of the subscripts are identical as in Eq. (1).

**Text S2.**

**Signal strength simulation**

This simulation seeks to establish the relationship between the water saturation level in the sand sample and its corresponding TA signal amplitude using the selected RPM. The 3D profile of the simulation model, which is identical to the experiment geometry, is described in Fig. S1. A rectangle waveguide filled with air is applied to excite the 1.3GHz microwave, and its dimension is $165mm \times 100mm \times 82.5mm$, the same as the WR650 waveguide used in the experiment. Moreover, the PEC (perfect electric conducting) boundary condition is specified at the waveguide, as indicated by the orange line in Fig. S1. The sand sample, whose dimension is $30mm \times 30mm \times 13mm$, is immersed in oil and lifted 40mm from the acrylic sheet layer. The scattering condition (red line in Fig. S1) is assigned to the oil boundary to mimic the PML (perfectly matched layer) conditions. The simulation is conducted using the COMSOL-Matlab client (V5.2).

The relationship between the water saturation level and the signal strength is evaluated by two parameters: the source strength and the peak-peak amplitude. The source strength is defined as $S(\mathbf{r}) = -\frac{\beta(\mathbf{r})}{C_p(\mathbf{r})}\sigma(\mathbf{r})||E^2(\mathbf{r})||$, in which $\beta(\mathbf{r})$ is the thermal expansion rate, $C_p(\mathbf{r})$ is the specific heat capacity, $\sigma(\mathbf{r})$ is the electric conductivity, and $E(\mathbf{r})$ is the electric field. The source strength is computed by treating the sand box as a monopole source, and the volume average of the target is applied. Meanwhile, in order to compute the peak-peak amplitude, the sand box can be discretized into $N_b$ elements with $S(\mathbf{r}_i)$ denoting the source strength for each element. Equation 3 is applied to obtain the received pressure profile $p(\mathbf{r}, \omega_a)$, in which $\omega_a$ and $k_a$ are the angular frequency and wave number of the TA wave, separately. The corresponding peak-peak amplitude is obtained after the inverse Fourier operation of $p(\mathbf{r}, \omega_a)$.

$$p(\mathbf{r}, \omega_a) = \sum_{i=1}^{N_b} \frac{S(\mathbf{r}_i)}{|\mathbf{r} - \mathbf{r}_i|} e^{-jk_a|\mathbf{r}-\mathbf{r}_i|} \tag{3}$$

**Text S3.**

**Sand box experiment**

This experiment is conducted to validate the relationship between the water saturation level and the corresponding TA amplitude. The system for measuring the TA signals generated by the sand boxes with different saturation levels is shown in Fig. S2a. A pulse lasting $1\mu s$ with 250Hz repetition rate is generated by the trigger source (Siglent SDG6000), and the microwave of 1.3GHz is excited by the microwave source (Hittite HMC-T2770). These two signals are transmitted through the microwave amplifier (AR 8000SP1z2G1z4M3), reaching a power of 2kW. The sand sample is placed in an oil bath, and the microwave is excited through a waveguide (WR650) to illuminate the sand box. A single-element transducer (Olympus A301) is used to collect the generated TA signal from the sand sample. Later, the TA signal is filtered by the ultrasound receiver (JSR DPR300) and displayed on an oscilloscope. The cable connection pattern for the devices is shown in Fig. S2b.

**Text S4.**

**Water distribution imaging experiment**

The experiment of water distribution imaging investigates the process of water infiltration into the dry sand cell using our proposed TA imaging techniques. The TA signal excitation system remains the same as the sand box experiment, but different transducer scanning platform and samples are used. As seen in Fig. S3a, the transducer is assembled on a

2D scanning platform that can run a raster scan in the X-Y plane. The linear encoder is also applied to the motion system, and a closed-loop control pattern is programmed to guarantee the precise measurement location. Moreover, the scanning platform also guarantees close contact between the transducer and the oil tank. The waveguide is placed at the back side of the sand cell, as shown in Fig. S3b. Figure S3c plots the sand sample from the top view. Two sand enclosures are prepared, and the thickness of the sand enclosure, which is 6.5mm, is smaller than the thickness of the sand cell. Moreover, the sand enclosure is closely attached to the front boundary of the sand cell, leaving no space for the air gap.

The temporal evolution of the water infiltration process is shown in Fig. S4. The fully saturated sand in the left enclosure is prepared as the reference marker, as displayed in Fig. S4a. For the first stage of this experiment, 1.5mL blue-dyed water is injected from the top into the right enclosure, and the water concentrates on the top of the enclosure, as shown in Fig. S4b. In order to avoid the Doppler effect, the raster scan of the transducer is conducted after the water profile stops developing. For the second stage of this experiment, three separate injections are attempted to fully saturate the right enclosure. The time separation between each injection and the injected water amount is presented in Table S1. Figures S4c-e show the photos for each separate injection in the second stage. It is observed that water goes to the bottom of the enclosure right after the first injection. The enclosure is sealed at the bottom, and this makes the fully saturated region to grow from the bottom to the top every time a new injection is made. Figure S4e shows the achieved fully saturated enclosure at the end of the experiment.

**Text S5.**

**Data processing**

The pressure profile of the received TA wave is converted to a voltage signal by the transducer and filtered by the ultrasound receiver. The transducer is fixed in the sand box experiment, and the TA pressure is measured at only one position. For the second experiment, the transducer conducts a raster scan for the dry sample, the fully saturated control marker enclosure on the left, and the two stages injecting water on the right enclosure. Thus, 4 sets of data are obtained for the second experiment. The collected data is named by the position of the transducer where it is measured. The amplifier power is also recorded to compensate for the power oscillation during the scan. The marker's image is obtained based on the difference between the dry sand and the marker. While the dynamic water distribution image is reconstructed based on the difference between the marker and the data collected in the corresponding experiment stage. Due to the mechanical misalignment, there is a sub-millimeter bias error in the Z-axis direction during the mechanical scanning. Hence, a compensation is made based on the arrival of the first peak in the measurement, which is generated by the front boundary of the sand cell. Moreover, a Hanning window is applied in the image reconstruction process.

**Text S6.**

**Imaging method**

The algorithm we used to reconstruct the image is derived from the governing equation Eq. (4). It is necessary to point out that Eq. (4) assumes that that the TA wave travels in an inelastic medium. The propagation of TA waves in the sand is not considered in the experiment of the letter. This assumption only holds when the propagation distance in the sand is small compared to the distance between the sand sample and the transducer. For the other situations where the TA wave travels a long distance inside the porous medium, Eq. (4) will be invalid, and the effects of velocity dispersion and amplitude attenuation should also be considered when transforming the equation to the frequency domain.

$$\nabla^2 p(\mathbf{r},t) - \frac{1}{c^2(\mathbf{r})}\frac{\partial^2}{\partial t^2}p(\mathbf{r},t) = -\frac{\beta(\mathbf{r})}{C_p(\mathbf{r})}\frac{\partial Q(\mathbf{r},t)}{\partial t} \tag{4a}$$

$$Q(\mathbf{r},t) \approx \sigma(\mathbf{r})||E(\mathbf{r})||^2 f^2(t) \tag{4b}$$

Equation 4 can be written in the frequency domain as follows:

$$\nabla^2 P(\mathbf{r},\omega_a) + k(\mathbf{r},\omega_a)^2 P(\mathbf{r},\omega_a) = -j\omega_a\frac{\beta(\mathbf{r})}{C_p(\mathbf{r})}\sigma(\mathbf{r})||\mathbf{E}(\mathbf{r})||^2(F(\omega_a) * F(\omega_a)), \tag{5}$$

where $P(\mathbf{r},\omega_a)$ is the TA pressure field in the frequency domain, and $\omega_a$ and $k(\mathbf{r},\omega_a)$ are the angular frequency and the wave number of the TA wave, respectively. $F(\omega_a)$ is the Fourier transform of the time domain modulation signal $f(t)$, and $F(\omega)*F(\omega)$ refers to the convolution of $F(\omega)$ with itself. Meanwhile, Eq. (5) can be regarded as an inhomogeneous Helmholtz equation, and the solution can be written as follows:

$$\frac{j}{\omega_a}\frac{P(\mathbf{r},\omega_a)}{F(\omega_a) * F(\omega_a)} = \int_V G(\mathbf{r},\mathbf{r}',\omega_a)\frac{\beta(\mathbf{r}')}{C_p(\mathbf{r}')}\sigma(\mathbf{r}')||E(\mathbf{r}')||^2 d\mathbf{r}' \tag{6}$$

where $G(\mathbf{r},\mathbf{r}',\omega_a)$ is the unknown heterogeneous Green's function. A common assumption is to replace the Green's function $G(\mathbf{r},\mathbf{r}',\omega_a)$ with the a known background approximation of the Green's function $G_b(\mathbf{r},\mathbf{r}',\omega_a)$, which is computed in the absence of the target.

According to Eq. (6), it is reasonable to suggest that the TA amplitude is directly proportional to the source term $\frac{\beta(\mathbf{r})}{C_p(\mathbf{r})}\sigma(\mathbf{r})||\mathbf{E}(\mathbf{r})||^2$. In addition, the left-side operation of Eq. (6) guarantees that the reconstructed source term is independent of the modulation signal. In this regard, different excitation patterns have been studied to improve the SNR (Signal to Noise Ratio) of the TA wave measurements. In order to solve Eq. (6), the imaging domain is discretized into $N = N_{row} \times N_{col}$ pixels, where $N_{row}$ and $N_{col}$ represent the number of pixels in rows and columns, separately. Correspondingly, the measurements $\mathbf{b}$ are collected by $N_{rcv}$ receivers sampled at $N_{fr}$ frequencies. Hence, the total number of measurements is $M = N_{rcv} \times N_{fr}$. The sensing matrix $A \in C^{(M \times N)}$ is composed of a discretization of the background field's Green's function. Hence, Eq. (6) can be written in the following form:

$$\mathbf{A}\chi = \mathbf{b}, \tag{7}$$

where $\chi = \frac{\beta(\mathbf{r}_n)}{C_p(\mathbf{r}_n)}\sigma(\mathbf{r}_n)||E(\mathbf{r}_n)||^2 (n = 1, 2, 3, ..., N)$ represents the unknown contrast variable discretized in the imaging domain. In a typical imaging scenario, the number of measurements is usually less than the number of unknowns, namely $M < N$, making that Eq. (7) has non-unique solutions. In this work, a complex conjugate pseudo-inverse approach is used to get the value of contrast variable.

**Text S7.**

**Estimation of the water saturation level**

The original images sliced at Z = 118mm for the marker, first injection, and last injection are shown in Figs. S5a-c, separately. It is observed that these images have identical profiles to the estimated water distribution results, which are presented in Figs. S5d-f, except the colorbar. Several assumptions made here to estimate the water saturation level in the sample. First, the relationship between the signal strength and water saturation level is approximated as a linear relationship for the sand box experiment. Second, the water saturation level in the marker is assumed to be 100% for the ground truth. The bottom part of the last injection is also treated as fully saturated. Fourth, the area of water-saturated sand also affects the image strength, which leads to the maximum image strength of the marker being more significant than that of the second injection. Such area factor is also compensated in the process of saturation level estimation.

**Text S8.**

**Scanning Speed**

Although the purpose of proposing the application of TA imaging is to conduct real-time imaging, the scanning process of the water distribution imaging experiment takes about one hour. A video showing the scanning speed is uploaded as part of the supplementary material. As shown in Movie S1, there are two reasons leading to the slow scanning speed. The first one is that only one transducer is used in the experiment, thus requiring a raster mechanical scan of the target. Another reason is that the time spend by the transducer at each position is about 2s, so that the signal to noise ratio can be improved by averaging samples. Therefore, the total scanning time is around 1h, considering the number of measurement points is 729 and the slow-moving speed of the transducer. In the future, other acoustics real-time imaging techniques, such as a multi-element transducer, will be applied to increase the scanning speed, and the maximum image frame rate should reach 0.5Hz.

**Movie S1.** The transducer conducting a raster scan during the experiment.

## References

Shen, L., Savre, W., Price, J., & Athavale, K. (1985). Dielectric properties of reservoir rocks at ultra-high frequencies. *Geophysics*, *50*(4), 692–704.

Troschke, B., & Burkhardt, H. (1998). Thermal conductivity models for two-phase systems. *Physics and Chemistry of the Earth*, *23*(3), 351–355.

Waples, D. W., & Waples, J. S. (2004). A review and evaluation of specific heat capacities of rocks, minerals, and subsurface fluids. part 1: Minerals and nonporous rocks. *Natural resources research*, *13*(2), 97–122.

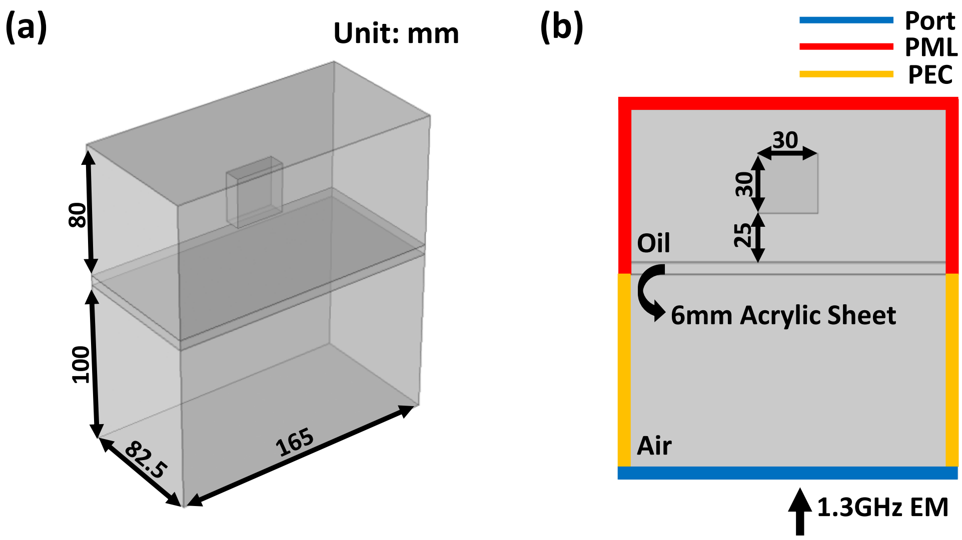


**Figure S1.** Simulation geometry for the relationship between signal strength and water saturation level: (a) geometry dimensions, and (b) boundary conditions

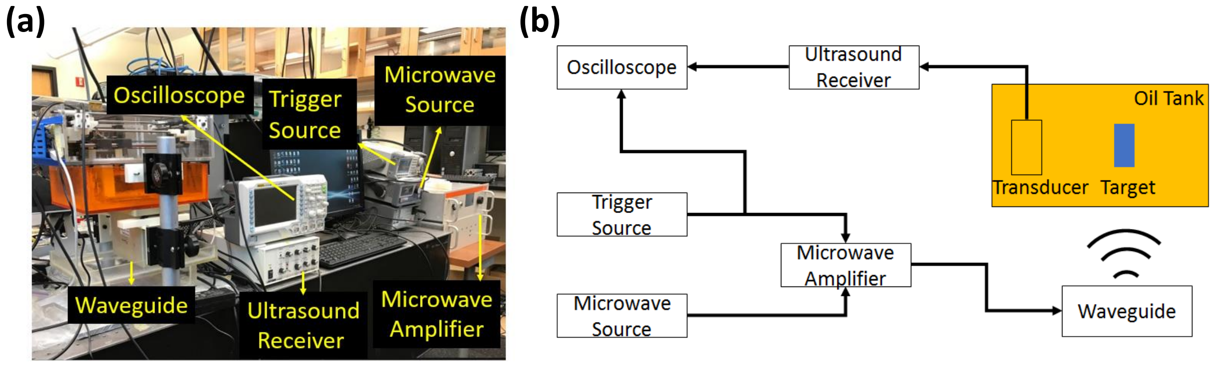


**Figure S2.** The testbed used to measure the TA signal generated by the sand box: (a) devices, and (b) the cable connection pattern.

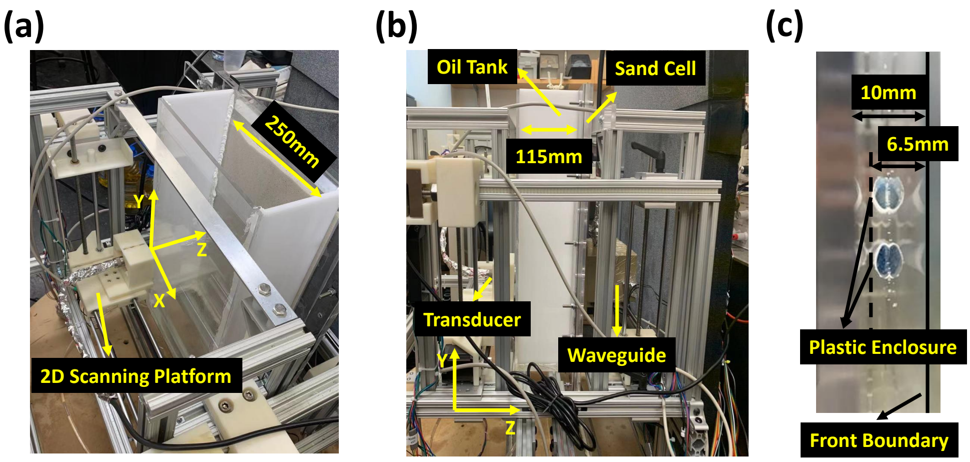


**Figure S3.** The testbed used to reconstruct the water distribution profile: (a) perspective view, (b) side view, and (c) the sand sample (top view).

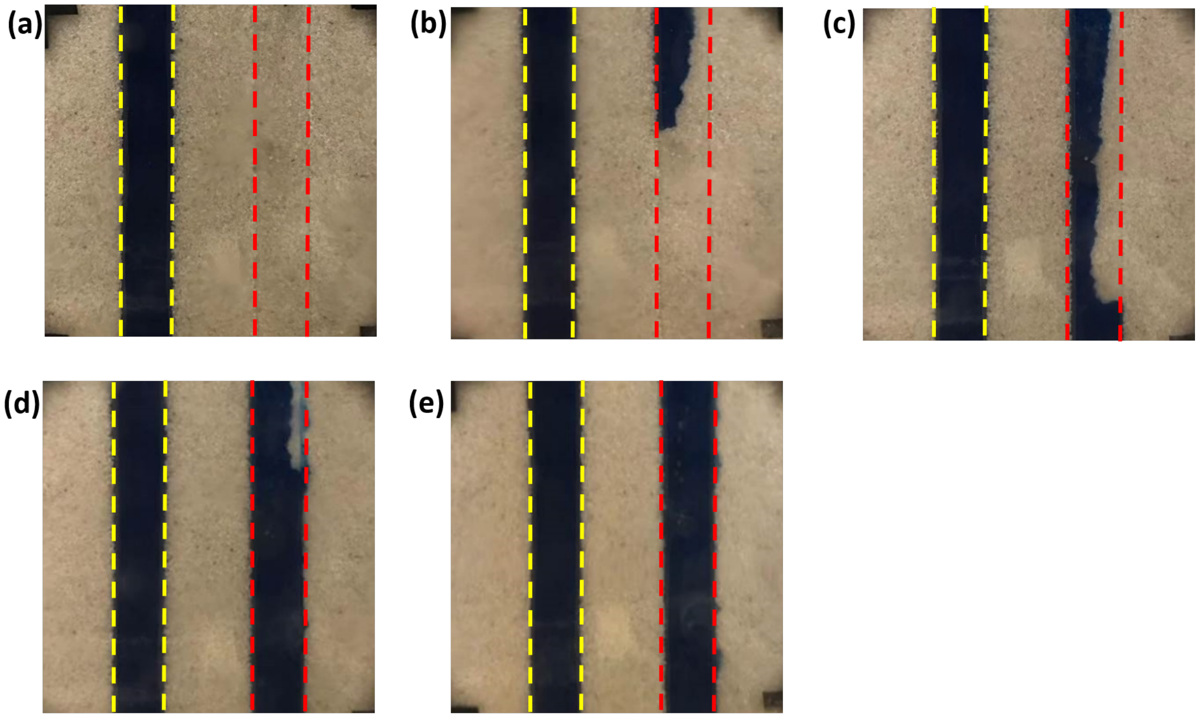


**Figure S4.** The water infiltration process: (a) the water distribution inside the marker (yellow dashed line), (b) the water distribution of the first stage experiment, the water distribution of the first (c), second (d), and third (e) injection in the second stage experiment.

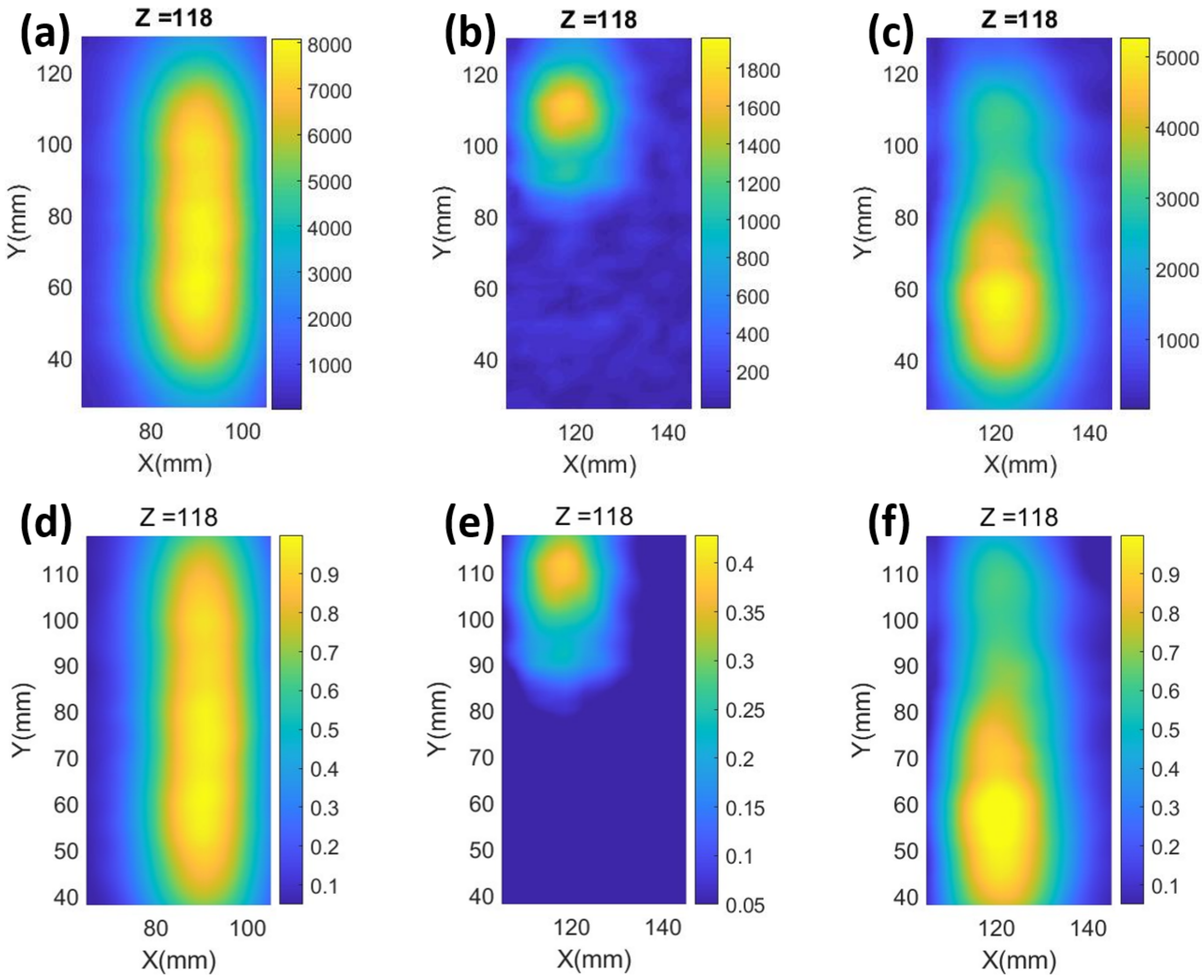


**Figure S5.** The obtained TA image for water distribution experiment: (a) original image of marker, (b) original image of the first stage, (c) original image of the second stage, (d) estimated water saturation level for marker, (e) estimated water saturation level for the first stage, and (f) estimated water saturation level for the second stage.

**Table S1.** Water Distribution Imaging Experiment: Water Injected Amount and Time Separation Between Two Successive Injections

| Stage | Injection Number | Time Separation (h) | Injected Amount (mL) |
|---|---|---|---|
| 1 | 1 | - | 1.5 |
| 2 | 1 | 2 | 1.2 |
| | 2 | 2.25 | 1.2 |
| | 3 | 2.25 | 1.5 |